Journal of
Micro/Nanolithography, MEMS, and MOEMS

SPIEDigitalLibrary.org/jm3

Wavefront-based pixel inversion algorithm for generation of subresolution assist features

Jue-Chin Yu
Peichen Yu
Hsueh-Yung Chao

Downloaded From: http://nanolithography.spiedigitallibrary.org/ on 04/24/2014 Terms of Use: http://spiedl.org/terms

Wavefront-based pixel inversion algorithm for generation of subresolution assist features

Jue-Chin Yu
Peichen Yu
National Chiao Tung University
Department of Photonics and Institute of Electro-Optical Engineering
1001 Da-hsueh Road
Hsinchu 30050, Taiwan
E-mail: yup@faculty.nctu.edu.tw

Hsueh-Yung Chao
ANSYS, Inc.
225 West Station Square Drive
Suite 200
Pittsburgh, Pennsylvania 15219

Abstract. The generation of subresolution assist features (SRAFs) using inverse-lithography techniques demands extensive computational resources which limits its deployment in advanced CMOS nodes. In this paper, we propose a wavefront-based pixel inversion algorithm to quickly obtain inverse masks with a high aerial image quality. Further assisted by a flexible pattern simplification technique, we present effective SRAF generation and placement based on the calculated inverse mask. The proposed approach can be easily inserted prior to a conventional mask correction flow for subsequent concurrent optimizations of both drawn patterns and SRAFs. The innovative pixel inversion and pattern simplification techniques allow quality mask corrections as produced by inverse lithography while maintaining the convenience of standardized/validated process flows currently used in the industry. © *2011 Society of Photo-Optical Instrumentation Engineers (SPIE).* [DOI: 10.1117/1.3663249]

Subject terms: optical proximity correction; inverse lithography; subresolution assist features.

Paper 11039PRRR received Mar. 29, 2011; revised manuscript received Oct. 4, 2011; accepted for publication Nov. 2, 2011; published online Dec. 1, 2011.

1 Introduction

Optical microlithography has been key to the semiconductor industry for more than 40 years. As the critical dimension (CD) of integrated circuit (IC) layouts becomes even smaller, mask pattern configurations become more complicated. Furthermore, with the shrinking CD, linewidths in IC layouts are now far beyond the resolution of the standard optical working wavelength (193 nm). Therefore, correcting deviations arising from optical diffraction is the most important factor for enhancing the yields of current optical lithographic systems. Resolution enhancement techniques (RETs) is a specialized field that combines optical principles and engineering technologies to compensate for the deviations from optical diffraction and therefore, improve image formation in lithography.[1,2]

Among available RETs, optical proximity correction (OPC), which is a mask alteration technique that compensates image intensity on the edges of drawn features,[3–6] is most essential and critical to the lithographic success of IC layers. The semiconductor industry has employed segment-based OPC for many generations and achieved some degree of success due to the straightforward implementation of iterative OPC algorithms. In general, such techniques first dissect the edges of drawn patterns into a collection of segments, where evaluation points are placed. After simulating the image formation by aligned optical models, the segments will be pulled in or pushed out according to the calculated image intensity at every evaluation point.[7] Because segment-based OPC only performs the correction by modifying existing layout edges, it is possible that patterns with problems related to subwavelength CDs, edge-placement errors (EPE), depth of focus (DoF), and mask error-enhancement factor (MEEF) (parameters usually used to evaluate the mask quality) cannot satisfy the specifications due to the limited solution space. To alleviate this issue, the current industry approach is to employ subresolution assist features (SRAFs) surrounding the main patterns to enhance the optical resolution.[8,9] Due to the quasiperiodical configurations formed by SRAFs and the main pattern, the diffractive light from the SRAFs can constructively interfere with the main images to adequately eliminate optical diffraction loss when segment-based OPC by itself is not sufficient. Therefore, problems like EPE, DoF, MEEF, and so on can then be improved. However, to prevent SRAF generation from being too time-consuming, ruled-based approaches are still the norm in the industry.[7] Such approaches use simple squares and rectangles, and require intensive experimentation on a variety of drawn layouts to create an explicit data base. With this, SRAFs can be quickly generated by looking up the data base according to the raw mask configurations, thereby reducing the SRAF generation time.

Nevertheless, as the IC manufacturing processes continue their progress toward the 32 and 20 nm nodes, CD becomes approximately one-tenth of the working wavelength. Under such conditions, rule-based SRAF generation is not sufficient to eliminate all the distortions from severe optical diffraction. Thus, in recent years another resolution enhancement technique known as inverse lithography (IL) or inverse mask technology has been proposed.[10–15] IL is a technique that theoretically calculates/corrects the full mask to compensate for strong image distortion from optical diffraction loss. IL calculates the full mask correction using a nonlinear regression that incorporates the inverse optimization algorithm to obtain a theoretically optimal mask after an elaborate computation. Many parameters related to fabrication can be factored into the calculation, such as the illumination source, projection system response, chemical resist reaction, etc. In addition, the generation of SRAFs and the correction of main patterns are usually optimized simultaneously. As a result, contrasting to

1932-5150/2011/$25.00 © 2011 SPIE

Downloaded From: http://nanolithography.spiedigitallibrary.org/ on 04/24/2014 Terms of Use: http://spiedl.org/terms

conventional OPC with rule-based SRAFs, a mask corrected by IL has higher pattern fidelity where EPE, DoF, MEEF and other mask evaluation parameters are much improved. Although IL-corrected masks have better image performance than those generated by OPC with rule-based SRAFs, the convolved and time-consuming calculation required by IL still presents a challenge in practice.

Since the introduction of the inverse problem formulation for optical microlithography by Sayegh, Nashold and Saleh,[16,17] many pixel-based inversion algorithms, considering coherent, incoherent, and partially coherent optical systems, have been demonstrated.[18,19] The inverse problems have been solved by linear programming, quadratic programming, or nonlinear formulations based on the assumptions made for the optical systems.[20–23] Recently, the traditional pixel-flipping techniques have been replaced with elaborated algorithms such as gradient descent methods[24,25] and level-set[26,27] alorithms, which have also been demonstrated on large-scale layouts. Although pixel-flipping techniques could also be very efficient for inverse lithography, the techniques exhibit some known issues. First, solutions can get easily stuck in local minima. Second, the resulting masks are randomly pixelated, and require refinement or post-processing for manufacturability. To address this problem, we develop an innovative pixel-flipping algorithm where the pixel-flipping is biased by a wavefront expansion technique.[28] We further incorporate a wavefront-based damping scheme and demonstrate that the resulting masks are similar to those obtained by more elaborated algorithms. For its application as a pre-OPC flow, a single iteration is often sufficient to generate SRAFs and to determine the bias of main features.

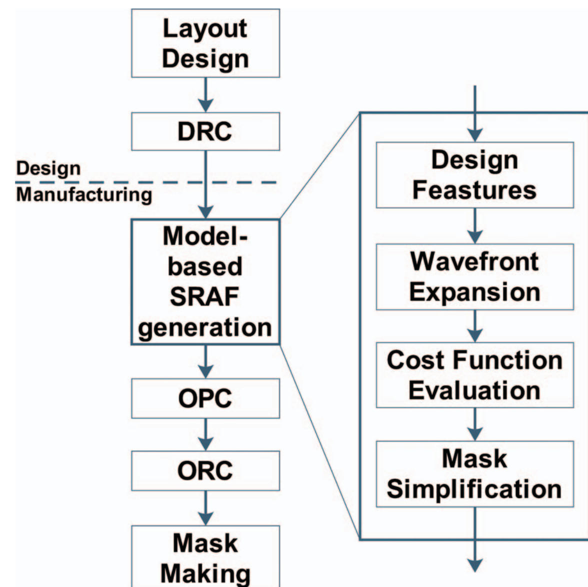

Fig. 1 Modified design/manufacturing flow with the insertion of model-based SRAFs and sizing using an inverse lithography algorithm. DRC: Design-rule check. OPC: Optical-proximity correction. ORC: Optical-rule check.

2 Methodology

In this paper we propose the generation of model-based SRAFs using an innovative IL algorithm before applying a conventional OPC flow. The IL algorithm employs a wavefront-based pixel flipping method which enables the correction of masks with CDs beyond the working wavelength in an acceptable time period. In this approach, all pixels on the mask are re-indexed according to the geometrical distributions of the input layout. In other words, an index is assigned to every pixel in accordance with their distance to the pattern edges. Thus, the edge pixels of all mask structures have the same index, with smaller indices corresponding to pixel locations near to the geometrical centers of the drawn patterns. Conversely, pixels far away from the patterns are given larger index values. Using such an index map allows the pixels to be processed in order as the wavefront propagates from the inside to the outside. All pixels with the same index n are corrected (flipped) at the same time, before processing the pixels with the subsequent higher index $n + 1$. Compared to the completely random flipping algorithms, the SRAF configurations generated with the wavefront-based approach are evidently more symmetrical to the main patterns and arranged periodically. Such phenomena are consistent with the physics of optical image formations, and hence give rise to high pattern fidelity.

Moreover, to reduce stitching issues arising from processing a large sized mask by dividing it into many tiles, the cost functions also incorporate a wavefront-based damping mechanism which biases the SRAFs to concentrate near the main patterns and restrict their generation at the edges of the tile. Finally, to make the corrected patterns suitable for the insertion into a standard flow, an image processing technique is exploited to simplify the resulting inverse mask without too much loss in image quality. Hence, the challenge to implement an IL-like approach is reduced while keeping the high image performance of an IL-generated mask.

Figure 1 illustrates the mask manufacturing flow that incorporates the proposed IL SRAF generation to obtain a pre-corrected mask before the standard OPC flow. The operation can determine the initial configurations of SRAFs and sizing of main patterns on the mask, which are used as the input to a subsequent standard OPC process. Due to relatively relaxed specifications in the pre-OPC step, the wavefront-based pixel-flipping algorithm requires only one or two iterations for convergence. Nevertheless, the precorrected mask enables a better mask correction because it employed the full mask space to create the initial configuration for OPC. So after pattern simplification via image processing, the subsequent standard OPC flow can directly correct the preliminary mask with included SRAFs. Thus, a high pattern fidelity mask can be quickly obtained by this combination of IL and conventional OPC flows. In our simulations, we use a conventional illumination source at 193 nm wavelength with a numerical aperture of NA $= 0.7$ and a coherence factor of $\sigma = 0.7$. The lithographic models are developed based on the Köhler illumination method, following Hopkin's imaging equation[29,30] and the singular value decomposition of the transmission cross coefficients for the eigenfunction expansion of the aerial image.[7,30] The kernels are then converted to a look-up table format for fast convolution. Furthermore, the convolution values of each kernel are cached for individual pixels to speed up the computation.

Downloaded From: http://nanolithography.spiedigitallibrary.org/ on 04/24/2014 Terms of Use: http://spiedl.org/terms

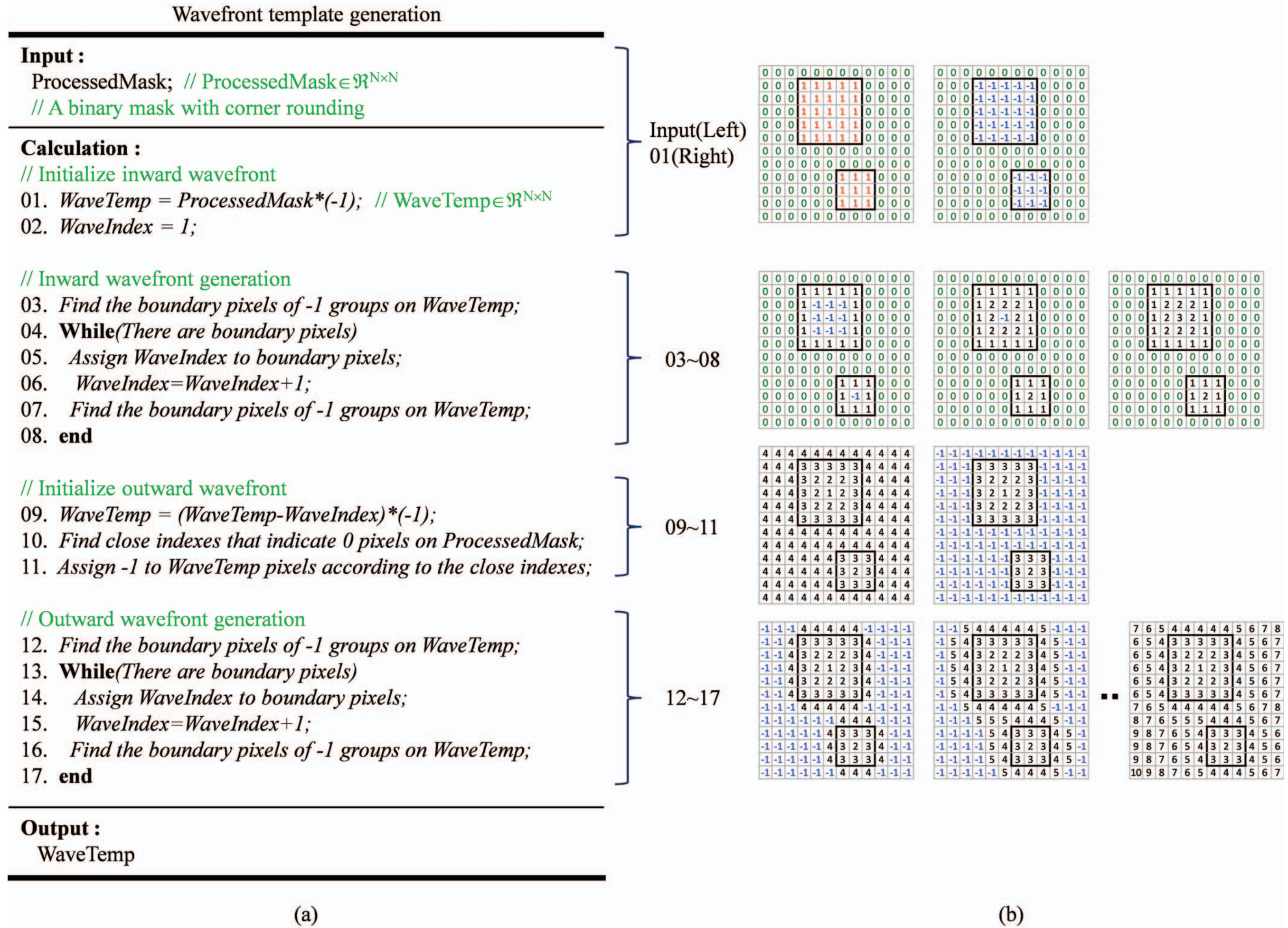

Fig. 2 (a) Pseudo-code of the wavefront template generation. (b) Illustrations of the wavefront evolution.

2.1 *Wavefront Expansion Technique*

At the core of our IL approach is a biasing technique based on a wavefront expansion. In this approach, all pixels on the mask are re-indexed according to the geometrical distributions of the input layout. In other words, an index is assigned to every pixel in accordance with their distance to the pattern edges. Thus, the edge pixels of all mask structures have the same index, with smaller indices corresponding to pixel locations near to the geometrical centers of the drawn patterns. Conversely, pixels far away from the patterns are given larger index values. Concretely, we construct a wavefront from the feature's edges both inwards and outwards for any particular layout. This way, we can construct a complete wavefront from a small region (or even a single point) inside each feature all the way to the margins of the tile. Figure 2 shows the pseudo-code with illustrations of the wavefront evolution at given steps of the algorithm.

A few examples of final wavefront templates are shown in Fig. 3. The topology of the wavefronts is induced by both the initial pattern and our choice of vicinity during the expansion (Manhattan), resulting in the "octagonal" shapes shown. These shapes are only an approximation to real propagation but the algorithm is efficient and able to capture the underlying optics, since our wavefront-based algorithm only biases the flipping (iteration) order, but in no way limits the final IL mask configurations. It is worth noting that this biasing technique will clearly identify pixels that are equidistant from two or more features. Once we have constructed the complete wavefront indices for a particular layout, denoted as the wavefront template, we proceed to evaluate pixels according to this order, from innermost to outermost. A key procedure in our IL approach is that all the pixels in any particular index are evaluated before any change is propagated to the mask. In other words, for each "ring," we evaluate if flipping a particular pixel is beneficial according to the cost function, but we do not immediately propagate this change. Only when all the pixels in a given index have been evaluated, they are all updated at the same time, and considered in the cost function for the next wavefront index. This will bias the final mask toward configurations that are center symmetric to the drawn patterns. Figure 4 illustrates the inverse calculation flow in a single iteration. Moreover, to compensate for the increasing size of the wavefronts as they move toward the edge of the layout, we introduce the concept of wavefront-based damping, as described in Sec. 2.2. In a nutshell, this technique assigns a decaying weight to wavefronts that are large but should not have a large influence on the final target image for being far away from the features.

Downloaded From: http://nanolithography.spiedigitallibrary.org/ on 04/24/2014 Terms of Use: http://spiedl.org/terms

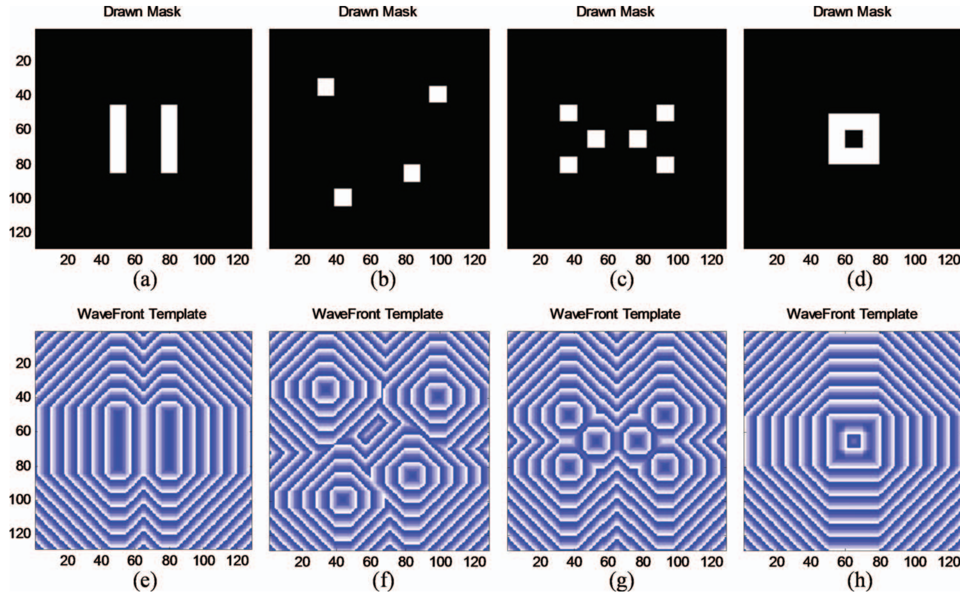

Fig. 3 Wavefront templates for various masks: (a) a pair of poly bars with a dimension of 100 nm × 400 nm separated by 200 nm, (b) four randomly placed contact holes with the same dimensions of 100 nm × 100 nm, (c) an SRAM unit cell composed of six contact holes with the same dimension of 100 nm × 100 nm, and (d) a square donut with a width of 300 nm and an opening with an area of 100 nm × 100 nm; (e)–(h) the corresponding wavefront templates for (a)–(d), respectively. For illustration purposes we repeat wavefronts from dark deep color to white but the corresponding indices increase strictly monotonically.

2.2 *Cost Functions and Wavefront-Based Damping*

Inverse lithography is an optimization problem[31,32] that tries to find the mask which generates an aerial image that deviates the least from a given target. The process of solving the problem involves three distinct parts: 1. the determination of a target image or contour, 2. a cost function that evaluates how far a given mask is from generating the desired target, and 3. an algorithm to search for candidate masks. The last part was described in Sec. 2.1. Here we address the first two. The target aerial images are constructed from drawn features, where sharp corners and edges are smoothed to facilitate the convergence of the optimization problem. Moreover, the image intensity along the edges of drawn features is set to the constant threshold at which we desire the contours to print.

In our simulations, the threshold image intensity for the photoresist is normalized to 0.5. With this, the target image for our IL calculation can be formulated by Eqs. (1) to (3),

$$\mathbf{\Phi}(i, j) = \text{TarMin}, \tag{1}$$

$$\mathbf{\Phi}(i, j) = (\text{EI} - \mathbf{W}(i, j) + 0.5)\frac{(\text{TarMax} - \text{TarMin})}{2\text{TD}} + 0.5, \tag{2}$$

$$\mathbf{\Phi}(i, j) = \text{TarMax}, \tag{3}$$

$$\text{W}(i, j) > \text{EI} + \text{TD}, \quad \text{EI} - \text{TD} < \text{W}(i, j) \le \text{EI} + \text{TD}, \quad \text{W}(i, j) \le \text{EI} - \text{TD},$$

where $\mathbf{\Phi}$ is the target image, $\mathbf{W}$ is the wavefront index configuration, EI is the edge index value, TD is the target depth, TarMin is the minimum value of target and TarMax is the maximum value of the target. $\mathbf{\Phi}$ and $\mathbf{W} \in \mathbf{R}^{N\times N}$ where N is the layout size in both row and column directions. i and j denote the row and column indexes of every entry of the matrixes. Figure 5 specifically illustrates the target image generated from Fig. 3(a) by our formulation. TarMin, TarMax, and TD are set to 0.2, 0.8, and 1, respectively. The same settings are used in all of the following simulations.

Our cost function is defined by two major parts. As seen in Eq. (4), the first part measures the intensity differences between the target aerial image and the one generated by a given mask. The second part, shown in Eq. (5), measures the accumulated intensity differences along target contours. Both parts are assigned proper weights to achieve a balance between adequate image contrast and desired contours. The optimization algorithm is then driven to minimize the cost function as the total summation, shown in Eq. (6). To summarize, our cost function has the following form:

$$F_{\text{image}} = w_{\text{image}}\Omega(p)\sum_{i=1}^{N}\sum_{j=1}^{N}|f[\Psi(i, j)] - \Phi(i, j)|, \tag{4}$$

$$F_{\text{contour}} = w_{\text{contour}}\Omega(p)\sum_{k=1}^{M}|f[\Psi(z_k)] - \Phi(z_k)|,$$
$$z_k = (i, j)_k, \tag{5}$$

$$F_{\text{image}} + F_{\text{contour}} \rightarrow \min. \tag{6}$$

F is the image and contour cost contributions, $\mathbf{\Psi}$ is the mask function, $f(\mathbf{\Psi})$ is the aerial image of a mask function, $\mathbf{\Omega}(p)$ is the damping coefficient of p's wavefront, $\mathbf{\Phi}$ is the target image, and w is the weights of the corresponding cost functions, where $f(\mathbf{\Psi}) \in \mathbf{R}^{N\times N}$. N is the layout size in both row

Downloaded From: http://nanolithography.spiedigitallibrary.org/ on 04/24/2014 Terms of Use: http://spiedl.org/terms

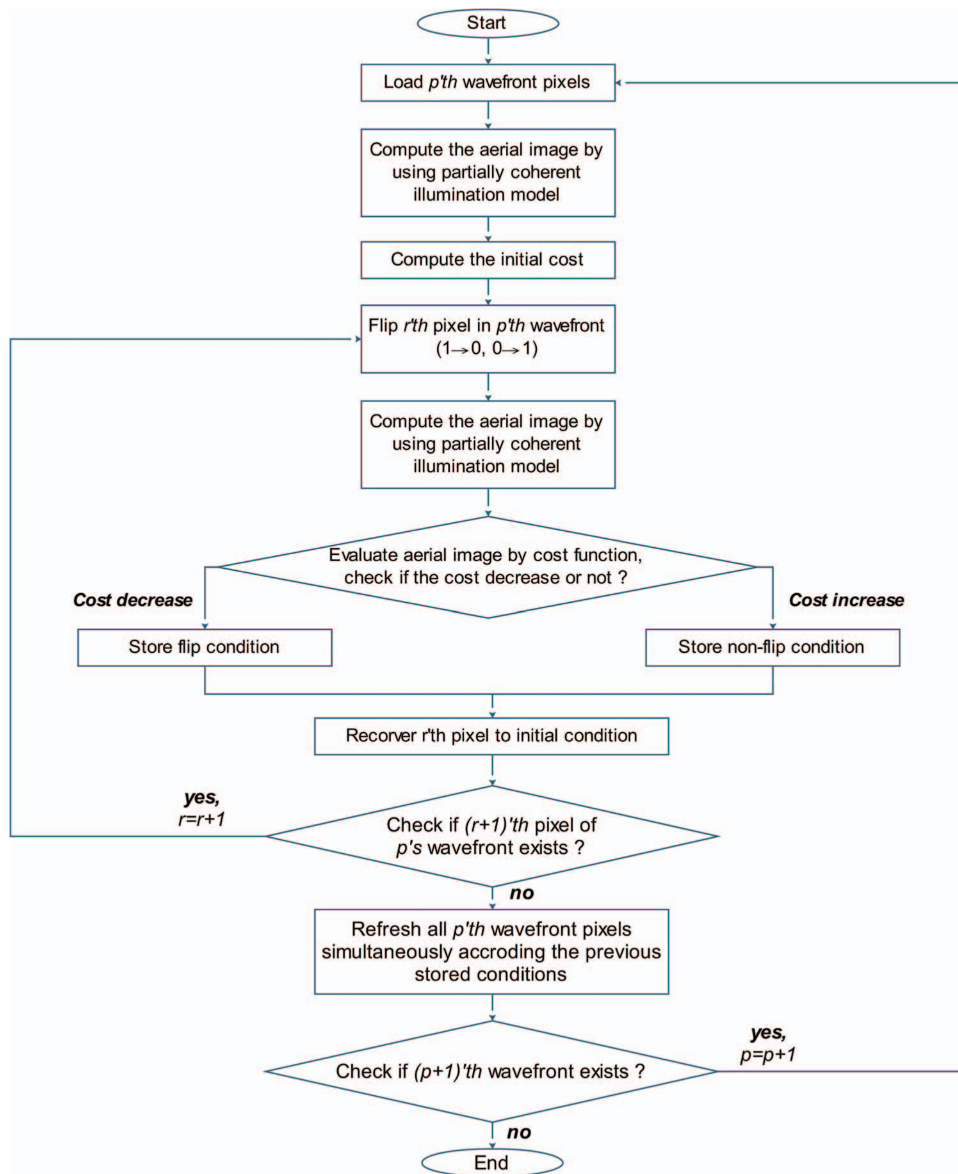

Fig. 4 The wavefront-based inverse calculation flow.

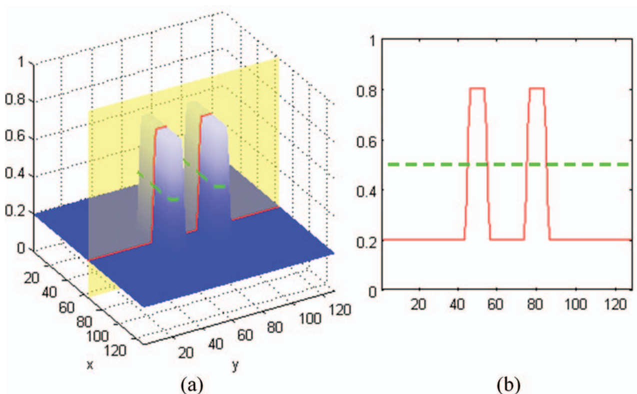

Fig. 5 (a) The target image for Fig. 3(a). (b) Cross section profile at $x = 64$. The dashed lines denote the threshold level and the solid lines the final target image.

and column directions, and M is the number of pixels which correspond to the target contour.

Moreover, it is worth noting that we introduce a wavefront damping coefficient in the cost function. The coefficient is determined based on the wavefront indices of individual pixels. We will show later that this technique effectively eliminates undesired patterns generated far away from the drawn features. This is an important result, as it minimizes the SRAF conflicts occurring on tile boundaries.

2.3 *Mask Simplification*

There are several ways to simplify the IL-generated mask patterns into regular polygons (rectangles). We choose a technique based on central moments.[33] The algorithm is as follows:

Downloaded From: http://nanolithography.spiedigitallibrary.org/ on 04/24/2014 Terms of Use: http://spiedl.org/terms

1. Extract all the connected components (clusters) from the input image.
2. Filter out small, negligible clusters by size.
3. Approximate the orientation and size of these clusters using central moments.
4. Snap results to manufacturable rectangles with edges at 45° or axis-aligned.

In order to extract all the connected components from the pixelated IL image, we use a binary segmentation technique. The technique is a one-pass, line-sweep algorithm that "builds" clusters one row at a time. The end result is a collection of separate regions whose union is equal to the original image. After this procedure is complete, we filter out small clusters that can be safely ignored due to their small size and consequently small influence.

Next, we consider each cluster individually and extract shape information using the statistical property of central moments. Each cluster can be considered to be a probability distribution, and as such, we compute the cluster's moments as:

$$\mu_{pq} = \sum_x \sum_y (x - \bar{x})^p (y - \bar{y})^q I(x, y), \tag{7}$$

where x and y are pixel coordinates and I is the image function for one particular cluster. The central moments are defined as:

$$\mu'_{20} = \frac{\mu_{20}}{\mu_{00}} = \frac{M_{20}}{M_{00}} - \bar{x}^2, \tag{8}$$

$$\mu'_{02} = \frac{\mu_{02}}{\mu_{00}} = \frac{M_{02}}{M_{00}} - \bar{y}^2, \tag{9}$$

$$\mu'_{11} = \frac{\mu_{11}}{\mu_{00}} = \frac{M_{11}}{M_{00}} - \bar{x}\bar{y}. \tag{10}$$

M_{pq} is the raw image moment defined as

$$M_{pq} = \sum_x \sum_y x^p y^q I(x, y). \tag{11}$$

With these, we can construct the covariance matrix for each cluster:

$$\mathrm{cov}[I(x, y)] = \begin{bmatrix} \mu'_{20} & \mu'_{11} \\ \mu'_{11} & \mu'_{02} \end{bmatrix}. \tag{12}$$

It is well-known that the eigenvectors of this matrix correspond to the major and minor axes of the probability distribution, or in our case, a single cluster. It is also known that the eigenvalues are proportional to the square of the main dispersion (cluster axes). We know the cluster size (pixel count) and therefore can scale the eigenvalues while maintaining their relative magnitudes.

With the eigenvectors and scaled eigenvalues we can create a rectangle for each cluster that has the same area and is aligned in the same way according to the dominant dispersion. Furthermore, we can snap each line segment to be either axis-aligned or at 45° for mask manufacturability.

3 Results and Discussion

In this section, we compare the optimized masks generated with and without the incorporation of the wavefront-based damping. As shown in Figs. 6 and 7, the examples presented include a. a pair of polybars with a dimension of 100 nm × 400 nm separated by 200 nm, b. four randomly placed contact holes with the same dimensions of 100 nm × 100 nm, c. an static random access memory (SRAM) bit composed of six

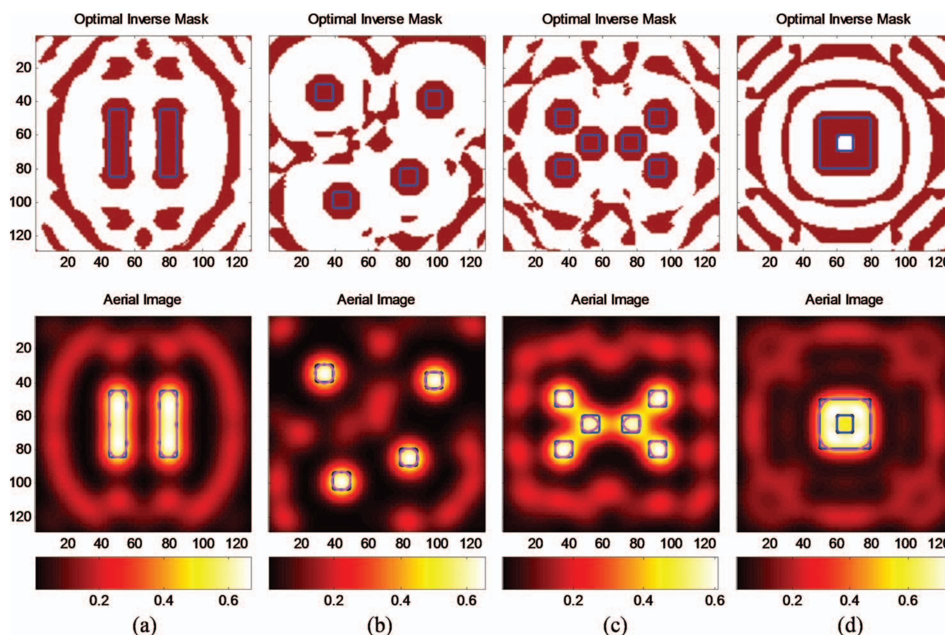

Fig. 6 The optimized masks and corresponding aerial images are computed without wavefront-damping treatments. The drawn patterns are plotted in solid lines and printed contours in dashed lines. The examples presented include (a) a pair of poly bars with a dimension of 100 nm × 400 nm separated by 200 nm, (b) four randomly placed contact holes with the same dimensions of 100 nm × 100 nm, (c) a SRAM unit cell composed of six contact holes with the same dimension of 100 nm × 100 nm, and finally (d) a square donut with a width of 200 nm and an opening with an area of 100 nm × 100 nm.

Downloaded From: http://nanolithography.spiedigitallibrary.org/ on 04/24/2014 Terms of Use: http://spiedl.org/terms

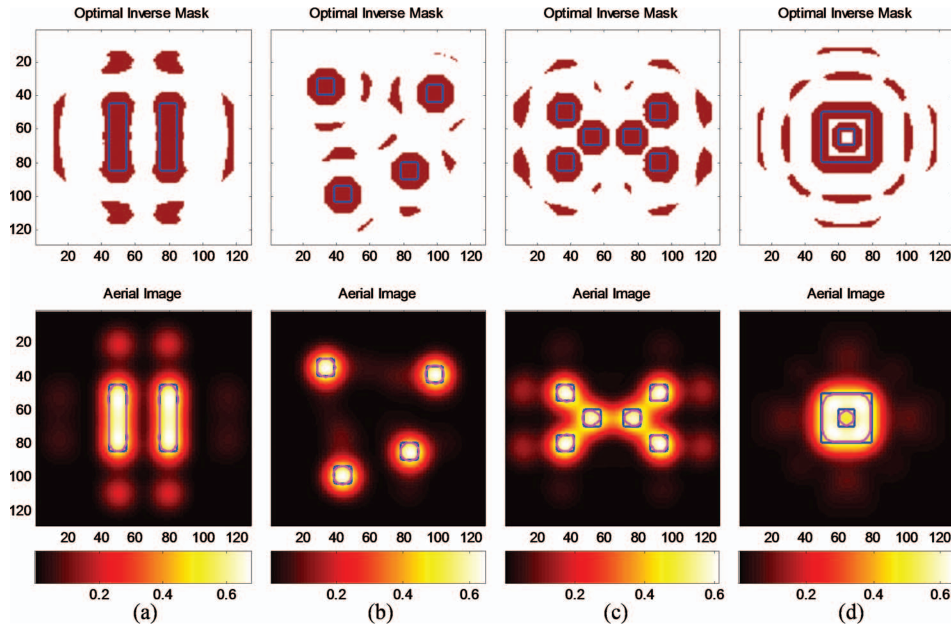

Fig. 7 The optimized masks and corresponding aerial images are computed with wavefront-damping treatments. The examples shown are the same as Fig. 6.

contact holes with the same dimension of 100 nm × 100 nm, and d. a square donut with a width of 300 nm and an opening with an area of 100 nm × 100 nm. The results are all computed in a single iteration with our algorithm. Afterwards, the simplification of IL-generated masks is demonstrated.

3.1 *Mask Optimization Without Wavefront-Based Damping*

As seen in Figs. 6(a)–6(d), the initial and calculated masks are shown in solid lines and burgundy patterns, respectively, while the calculated aerial images and contours are shown in color maps and dashed lines. First, we note that the main features are now surrounded by SRAFs forming rings. For an isolated feature, as seen in Fig. 6(d), the arrangement of mask patterns resembles octagons in shape, clearly determined by the wavefront expansion. The sizes of bright and dark SRAFs are determined by the model and hence could be big or small in shape regardless of position. The EPEs of different masks are satisfying to some extent, except that the center of the square donut in Fig. 6(d) does not print.

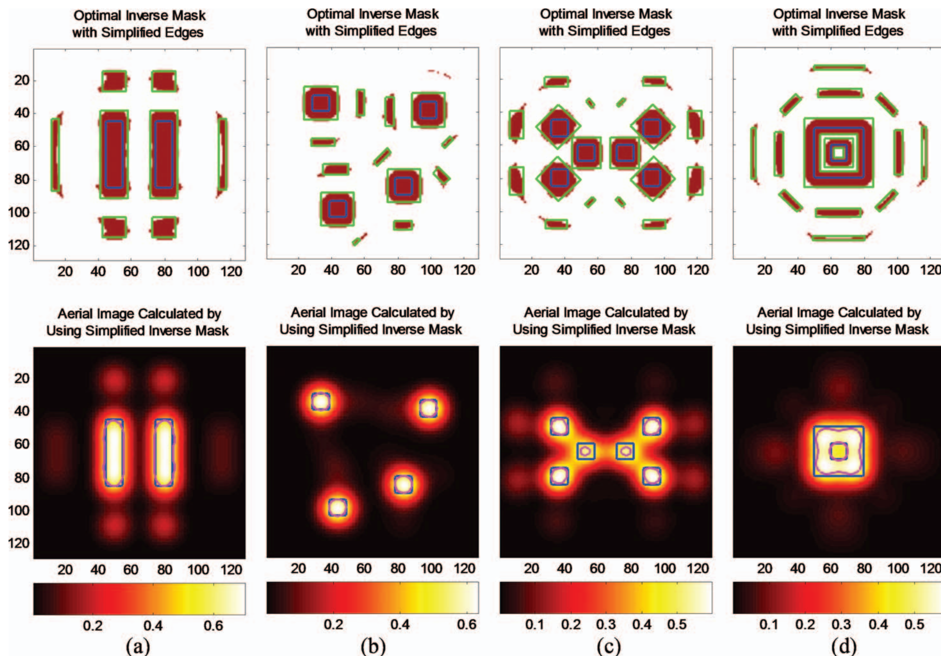

Fig. 8 The simplified mask templates of Fig. 7.

Downloaded From: http://nanolithography.spiedigitallibrary.org/ on 04/24/2014 Terms of Use: http://spiedl.org/terms

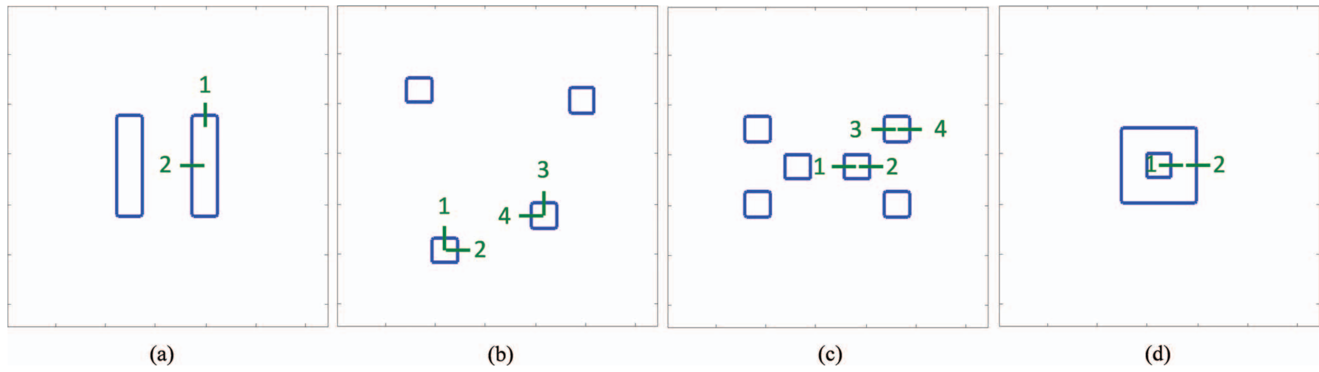

Fig. 9 The cut line configurations.

However, the aerial image contrast is limited due to the spreading distributions of SRAFs. These observations are not surprising since the entire layout is one of many potential candidate masks for an inverse lithography problem. Furthermore, it is commonplace that an optimization algorithm converges to a local minimum that may not best represent the desired solution. The wavefront-based damping introduced next allows the algorithm to quickly arrive near the vicinity of desirable IL solutions, obtaining results similar to other more elaborate algorithms.

3.2 *Mask Optimization with Wavefront-based Damping*

With an optimization algorithm that incorporates the wavefront-based damping, the computed masks show compact SRAFs and high image contrasts, as shown in Figs. 7(a)–7(d). Also, the contours print better than those generated without the damping, particularly shown in Fig. 7(d). We believe that the wavefront damping technique used in this pixel-flipping algorithm cannot only save computational time, but also reduces the tile stitching problem in large-scale layouts.

3.3 *Mask Simplification Example*

As described in Sec. 2.3, the inverse-generated masks can also be transformed into simple rectangles based on central moments. Figure 8 shows the examples of a. a pair of poly bars with a dimension of 100 nm × 400 nm separated by 200 nm, b. four randomly placed contact holes with the same dimensions of 100 nm × 100 nm, c. a SRAM bit composed of six contact holes with the same dimension of 100 nm × 100 nm, and d. a square donut with a width of 300 nm and an opening with an area of 100 nm × 100 nm. The optimized masks are the same as those presented in Fig. 7. In the top part of Fig. 8, the simplified edges of SRAFs and the main patterns are snapped into 45° and axis-aligned line segments

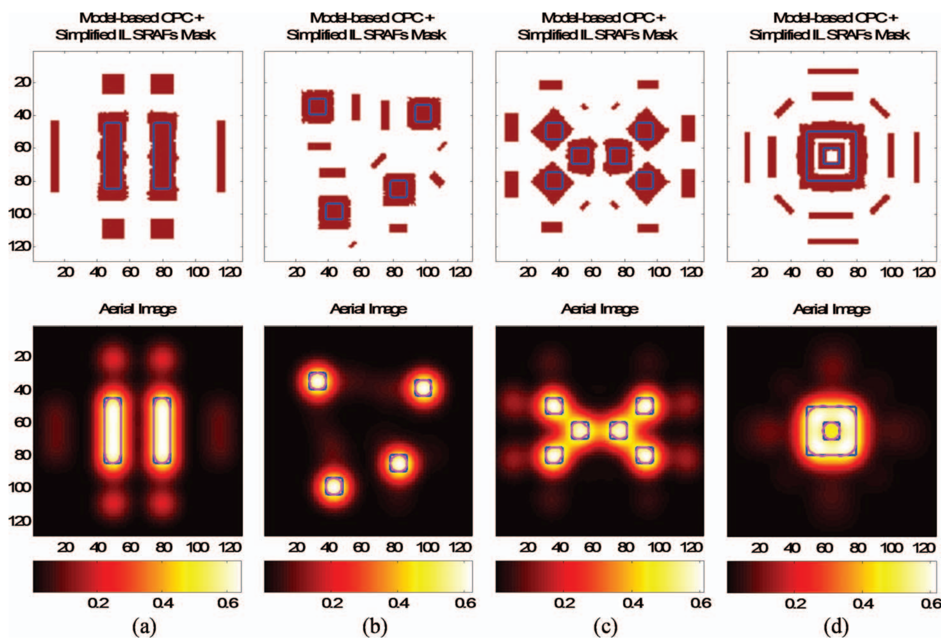

Fig. 10 The segment-based OPC results of the simplified mask templates given in Fig. 8.

Downloaded From: http://nanolithography.spiedigitallibrary.org/ on 04/24/2014 Terms of Use: http://spiedl.org/terms

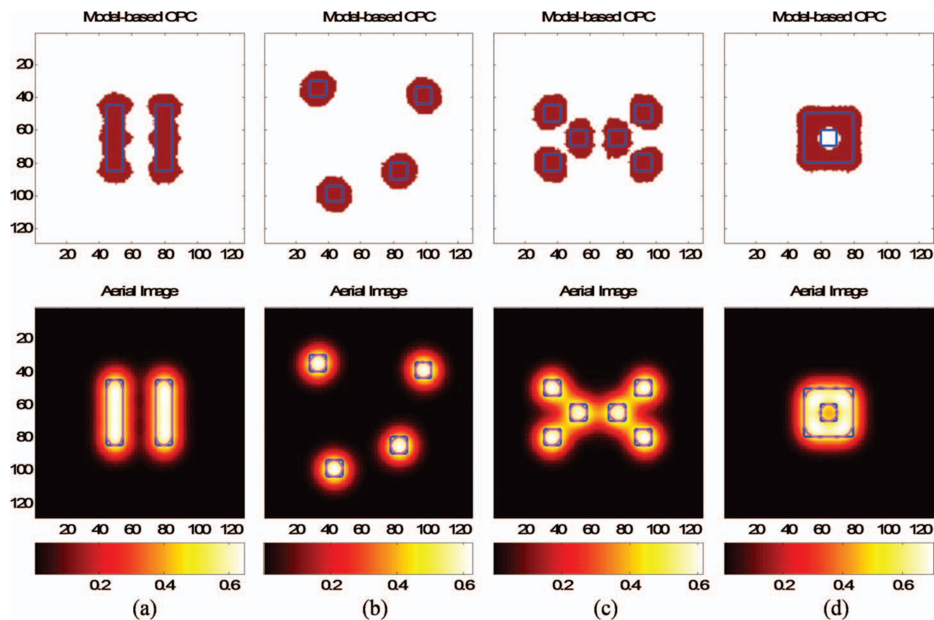

Fig. 11 The segment-based OPC results of the original drawn masks without the pre-OPC flow.

and plotted in solid lines. In a similar way the corresponding aerial images and printed contours (dashed lines) after mask simplification are shown on the bottom part of Fig. 8.

After simplification, the inverse calculated SRAFs are converted into rectangles with Manhattan placements. Such configurations are reasonable and usual in rule-based OPC flows. In the case of the four randomly placed contacts, shown in Fig. 8(b), the SRAFs are sandwiched between two biased contacts. Instead of axis-aligned line segments, the simplified SRAFs are placed in 45° orientations to accommodate the arrangement of two nearby contacts. Such SRAF placement would likely not have been generated with a simple rule-based procedure. Moreover, the impact of the mask simplifications on contours is also compared. Due to a conservative transformation from the automatically generated features, the printed contours present tiny mismatches and the contrasts of aerial images are slightly deteriorated compared to the unsimplified results. Figure 8(c) shows the simplified mask of the SRAM bit composed of six contacts. The space between nested contact holes does not allow the placement of any SRAFs, which is consistent with the optical diffraction limit when the separations are less than the dimensions of contacts. Moreover, as shown on the bottom part of Fig. 8(c), the simplified main patterns result in deteriorated pattern fidelity for the two center contact holes where the EPEs degrade obviously. Such phenomenon is not surprising because no SRAFs are present around these two contact holes to alleviate the impact of pattern conversion. However, this is not a fatal flaw as the mask simplification is only the pre-OPC output. The contours can be fine tuned later by the OPC correction of the main features. Finally, the simplified mask of an isolated square donut with SRAFs is shown in Fig. 8(d) with reasonable image contrasts and print contours. It is worth noting that the 45° SRAFs are generated at places that are not straightforward to rule-based procedures, validating this approach for model-based SRAF generation and placement.

In order to quantify the impact of the simplification process, the EPEs and the normalized-image-log- slope (NILS) values before and after mask simplification were calculated at the locations shown in Fig. 9, and summarized in Table 1. As seen in Table 1, the NILS values were not affected drastically by the process. However, the EPEs could deteriorate by as much as tens of nanometers in locations such as cut line 1 and 2 of Fig. 9(c). To validate our proposed approach for a pre-OPC flow, we need to incorporate segment-based OPCs on the main patterns to examine if the pattern fidelity is indeed recovered and improved.

We first run a segment-based OPC flow for main patterns of the simplified masks as shown in Fig. 8 using the same optical model. For simplicity, our algorithm employed the pixel unit, which is 10 nm, as the segmentation length and offset distance for the correction flow. The original drawn masks were also treated by the same OPC flow without the insertion of SRAFs for comparison. Figures 10 and 11 show the segment-based OPC results of the simplified masks generated by the pre-OPC flow and for the original drawn masks without pre-OPC, respectively. The calculated EPE and NILS values at locations shown in Fig. 9 are also summarized and compared in Table 2. It is evident that our proposed approach in the pre-OPC stage resulted in less EPEs after OPC at critical locations than those obtained by segment-based OPC only. The average EPE enhancement of all cut lines in the first three examples was 22.34% with a 1.93% decrease in NILS. The NILS values were slightly affected due to the insertion of SRAFs. However, in the example of a square donut, the average EPE enhancement was only 16.28% and the NILS was decreased by 30.42%. The phenomenon occurred because the donut pattern was split into two concentric parts in our current algorithm, which could be further improved in the future. Finally, we show that with our proposed pre-OPC flow, the corrected mask templates after OPC could still maintain manufacturing-friendly geometries. As seen in Fig. 10, the main patterns were close to conventional rule-based OPC

Downloaded From: http://nanolithography.spiedigitallibrary.org/ on 04/24/2014 Terms of Use: http://spiedl.org/terms

Table 1 The simulated EPE (in nanometers) and NILS (in AU) for the examples.

Cutline	1				2				3				4			
	EPE		NILS		EPE		NILS		EPE		NILS		EPE		NILS	
	Raw	Simplify	Raw	Simplify	Raw	Simplify	Raw	Simplify	Raw	Simplify	Raw	Simplify	Raw	Simplify	Raw	Simplify
Two bars	0.56	6.17	0.0785	0.0860	1.44	−6.14	0.0976	0.0986	–	–	–	–	–	–	–	–
4 random vias	−0.60	2.47	0.0835	0.0842	−0.48	2.28	−0.0838	−0.0831	−0.08	3.04	0.0848	0.0853	−0.07	3.02	0.0832	0.0835
SRAM bit	2.60	32.35	0.0500	0.0493	−5.38	24.56	−0.0502	−0.0478	0.29	7.05	0.0763	0.0764	0.13	5.81	−0.0805	−0.0795
Square donut	−7.84	3.51	0.0288	0.0291	8.76	21.96	−0.0649	−0.0749	–	–	–	–	–	–	–	–

Table 2 The calculated EPEs (in nanometers) and NILSs (in AU) after a segment-based OPC flow for the simplified masks generated by the pre-OPC flow and for the drawn masks without pre-OPC.

Cutline	1				2				3				4			
	EPE		NILS		EPE		NILS		EPE		NILS		EPE		NILS	
Pre-OPC flow	Yes	No	Yes	No	Yes	No	Yes	No	Yes	No	Yes	No	Yes	No	Yes	No
Two bars	−0.22	−1.56	0.0679	0.0686	0.28	−0.36	0.0965	0.0953	–	–	–	–	–	–	–	–
4 random vias	−0.42	0.15	0.0838	0.0881	0.16	−0.23	−0.0858	−0.0861	0.06	−0.05	0.0843	0.0869	−0.12	−0.43	0.0840	0.0855
SRAM bit	−2.25	−2.80	0.0497	0.0540	−0.95	−0.21	−0.0569	−0.0618	0.12	0.07	0.0721	0.0743	−0.1	−1.07	−0.0773	−0.0794
Square donut	1.34	2.14	0.0379	0.0567	0.83	0.79	−0.0596	−0.0824	–	–	–	–	–	–	–	–

Downloaded From: http://nanolithography.spiedigitallibrary.org/ on 04/24/2014 Terms of Use: http://spiedl.org/terms

results, while SRAFs were either Manhattans or snapped to 45°. Compared to the mask templates with segment-based OPC only, as shown in Fig. 11, the rounded shapes were rather not preferable for the mask making process. At the end, such mask geometries were results of severe diffraction in a low k_1 process condition, where the rounded mask patterns tended to be the local-minima solution in segment-based correction algorithms without any constraints.

4 Conclusion

In conclusion, we have demonstrated an innovative pixel-flipping technique for inverse lithography. By incorporating a wavefront-expansion and damping technique, we show that the generated mask patterns are suitable for model-based SRAF generation and placement. In this approach, the drawn patterns receive a model-based sizing with automatic SRAF generation, which are computed simultaneously in a single iteration. Our method generates compact SRAFs only near drawn features, which could be helpful in reducing tile stitching problems if applied at a full-chip scale. Finally, we demonstrate that the IL-generated masks can be simplified into simple polygons using central moments. Additionally, the insertion of IL in the pre-OPC stage results in minimal impact to the existing flows while providing many of the IL advantages. We believe that our proposal has great value because it provides an excellent starting point for any OPC flow currently in use, and in our experience, the final convergence of conventional OPC approaches—especially those based on gradient descent — depends greatly on good initial conditions.

References

1. F. M. Schellenberg, "Resolution enhancement technology - the past, the present, and extensions for the future," in *Proc. SPIE Optical Microlithography XVII*, Vol. 5377, p. 1 (2004).
2. J. F. Chen, V. D. B. Douglas, S. Hsu, M. C. W. Hsu, L. Tom, X. Shi, T. Chen, R. J. Socha, U. Hollerbach, K. E. Wampler, J. Park, S. Park, and K. Gronlund, "RET masks for the final frontier of optical lithography," in *Proc. SPIE Photomask and Next-Generation Lithography Mask Technology XII*, Vol. 5853, p. 168 (2005).
3. A. Gu and A. Zakhor, "Optical proximity correction with linear regression," *IEEE Trans. Semicond. Manuf.* **21**(2), 263–271 (2008).
4. P. Gupta, A. B. Kahng, C. H. Park, K. Samadi, and X. Xu, "Wafer topography-aware optical proximity correction," *IEEE TCAD.* **25**(12), 2747–2756 (2006).
5. K. Lucas, C. M. Yuan, R. Boone, K. Wimmer, K. Strozewski, and O. Toublan, "Logic design for printability using OPC methods," *IEEE Design & Test of Computers.* **23**(1), 30–37 (2006).
6. P. Yu, S. X. Shi, and D. Z. Pan, "Process variation aware OPC with variational lithography modeling," in *Proceedings of the 43rd ACM/IEEE Design Automation Conference*, pp. 785–790 (2006).
7. N. B. Cobb, "Fast optical and process proximity correction algorithms for integrated circuit manufacturing," Ph.D. dissertation, University of California, Berkeley, Berkely, California (1998).
8. A. B. Kahng, S. Muddu, and C. H. Park, "Auxiliary pattern-based optical proximity correction for better printability, timing, and leakage control,"*J. Micro/Nanolith. MEMS MOEMS* **7**, 013002 (2008).
9. P. Gupta, A. B. Kahng, and C. H. Park, "Detailed placement for enhanced control of resist and etch CDs," *IEEE TCAD.* **26**(12), 2144–2157 (2007).
10. J. Ho, Y. Wang, X. Wu, W. Leitermann, B. Lin, M. F. Shieh, and J. W. Sun, "Real-world impact of inverse lithography technology," in *Proceedings of the SPIE 25th Annual BACUS Symposium on Photomask Technology*, Vol. 5992, p. 59921Z (2005).
11. Y. Granik, "Fast pixel-based mask optimization for inverse lithography," *J. Microlithogr., Microfab., MicroSyst.* **5**, 043002 (2006).
12. L. Pang, Y. Liu, and D. Abrams, "Inverse lithography technology (IL): a natural solution for model-based SRAF at 45 nm and 32 nm," in *Proc. SPIE Photomask and Next-Generation Lithography Mask Technology XIV*, Vol. 6607, p. 660739 (2007).
13. M. L. Kempsell, E. Hendrickx, A. Tritchkov, K. Sakajiri, K. Yasui, S. Yoshitake, Y. Granik, G. Vandenberghe, and B. W. Smith, "Inverse lithography for 45-nm-node contact holes at 1.35 numerical aperture," *J. Micro/Nanolith. MEMS MOEMS* **8**, 043001 (2009).
14. E. Y. Lam and A. K. Wong, "Computation lithography: virtual reality and virtual virtuality," *Opt. Express* **17**, 12259–12268 (2009).
15. J. C. Yu and P. Yu, "Impacts of cost functions on inverse lithography patterning," *Opt. Express* **18**, 23331–23342 (2010).
16. B. E. A. Saleh and S. I. Sayegh, "Reductions of errors of microphotographic reproductions by optical corrections of original masks," *Optical Eng.* **20**, 781–784 (1981).
17. K. M. Nashold and B. E. A. Saleh, "Image construction through diffraction-limited high-contrast imaging systems: an iterative approach," *J. Opt. Soc. Am. A* **2**, 635–643 (1985).
18. X. Ma and G. R. Arce, "Binary mask optimization for forward lithography based on the boundary layer model in coherent systems," *J. Opt. Soc. Am. A* **26**, 1687–1695 (2009).
19. J. C. Yu, P. Yu, and H. Y. Chao, "Innovative pixel-inversion calculation for model-based subresolution assist features and optical proximity correction," in *Proceedings SPIE Optical Microlithography XXII*, Vol. 7274, p. 72743B (2009).
20. D. C. Sorensen, "Newton's method with a model trust region modification," *SIAM J. Numer. Anal.* **19**, 409–426 (1982).
21. A. E. Rosenbluth, R. N. Singh, S. Bukofsky, C. Fonseca, K. Lai, A. F. Molless, M. Hibbs, and A. K. K. Wong, "Optimum mask and source patterns to print a given shape," *J. Microlithogr., Microfabr., Microsyst.* **1**, 13–30 (2002).
22. D. Luenberger, *Linear and Nonlinear Programming*, Kluwer Academic Publishers, Norwell, Massachusetts (2003).
23. R. J. Socha, D. J. V. D. Broeke, J. F. Chen, T. L. Laidig, N. Corcoran, U. Hollerbach, K. E. Wampler, X. Shi, and W. Conley, "Contact hole reticle optimization by using interference mapping lithography (IML)," in *Proceedings SPIE Photomask and Next-Generation Lithography Mask Technology XI*, Vol. 5446, pp. 516–534, (2004).
24. A. Poonawala and P. Milanfar, "Double-exposure mask synthesis using inverse lithography," *J. Micro/Nanolith. MEMS MOEMS* **6**, 043001 (2007).
25. J. C. Yu and P. Yu, "Choosing objective functions for inverse lithography patterning," in *Proceedings SPIE Optical Microlithography XXIV*, Vol. 7973, p. 79731N (2011).
26. Y. Shen, N. Wong, and E. Y. Lam, "Level-set-based inverse lithography for photomask synthesis," *Opt. Express* **17**, 23690–23701 (2009).
27. Y. Shen, N. Jia, N. Wong, and E. Y. Lam, "Robust level-set-based inverse lithography," *Opt. Express* **19**, 5511–5521 (2011).
28. J. C. Yu, P. Yu, and H. Y. Chao, "Model-based subresolution assist features using an inverse lithography method," in *Proceedings SPIE Lithography Asia 2008*, Vol. 7140, p. 714014 (2008).
29. M. Born, and E. Wolf, *Principles of Optics*. 6th Ed, Pergamon Press, pp. 528–532 (1980).
30. A. K. K. Wong, *Optical Imaging in Projection Microlithography*, pp. 63–70, SPIE Press, Bellingham, Washington (2005).
31. Y. Liu and A. Zakhor, "Optimal binary image design for optical lithography," in *Proceedings of SPIE Optical/Laser Microlithography III*, Vol. 1264, pp. 401–412 (1990).
32. Y. Liu and A. Zakhor, "Binary and phase-shifting image design for optical lithography," in *Proceedings of SPIE Optical/Laser Microlithography IV*, Vol. 1463, pp. 382–399 (1991).
33. J. Flusser and T. Suk, "Rotation moment invariants for recognition of symmetric Objects," *IEEE Trans. Image Process* **15**, 3784–3790 (2006).

Jue-Chin Yu received his BSEE degree in the department of electrical engineering from National University of Kaohsiung (NUK) Kaohsiung, Taiwan and an MS degree in Institute of Photonic Technologies from National Tsing-Hua University (NTHU), Hsinchu, Taiwan, in 2004 and 2006, respectively. He is now advanced in studying PhD in the Institute of Electro-Optical Engineering at National Chiao-Tung University (NCTU), Hsinchu, Taiwan. His research interests are in inverse problem of RET for 32 nm lithography and beyond, which include IL and source-mask optimization. He worked at TSMC, Hsin-Chu, Taiwan, as a RET engineering intern in the summers of 2009 and 2010. He was the recipient of the best student paper awards in SPIE lithography Asia 2008 and SPIE advanced lithography 2010.

Downloaded From: http://nanolithography.spiedigitallibrary.org/ on 04/24/2014 Terms of Use: http://spiedl.org/terms

Peichen Yu received her PhD (2004) in electrical engineering from the University of Michigan, Ann Arbor. From 2004 to 2006, she was an RET design engineer for the advanced design group of Intel Corporation at Hillsboro, Oregon. In 2006, she joined the Department of Photonics and the Institute of Electro-Optical Engineering at National Chiao-Tung University at the rank of assistant professor and was promoted to associate professor in August 2009. Her research interests include the design and development of nanostructured solar cells and light emitting diodes. She is also actively engaged in the development of OPC and DFM solutions for CMOS 32 nm microlithography and beyond. She has published over 20 refereed technical papers in the above research areas. Her work has been selected for Virtual Journal of Nanoscale Science & Technology and highlighted by SPIE newsroom, NPG Nature Asia-Material, etc. She is a member of IEEE Photonics Society and SPIE and the recipient for 2010 Y. Z. Hsu Scientific Paper Award.

Hsueh-Yung (Robert) Chao received a BS degree from the National Sun Yat-Sen University, Kaohsiung, Taiwan, in 1994, and MS and PhD degrees from the University of Illinois at Urbana-Champaign, in 1998 and 2002, respectively. From August 1996 to December 2002, he was a research assistant at the Center for Computational Electromagnetics, University of Illinois at Urbana-Champaign. In 1999 and 2002, he held summer internships with Intel, Hillsboro, Oregon, where in 2003, he was a senior CAD engineer in the TCAD Department. In February 2004, he joined the Department of Communication Engineering, National Chiao Tung University, Hsinchu, Taiwan, as an assistant professor. From September 2008 to May 2011, he worked as a senior R&D engineer at Synopsys, Mountain View, California, on electromagnetic simulation of optoelectronic devices. Starting from June 2011 he worked as a lead R&D engineer at ANSYS, Pittsburgh, Pennsylvania, on HFSS Transient. His current research interests include computational electromagnetics, optical imaging in microlithography, and parallel computing. He was the recipient of the Spontaneous Recognition Award from Intel in 2003 and the Excellence in Teamwork Award from Synopsys in 2009.

Downloaded From: http://nanolithography.spiedigitallibrary.org/ on 04/24/2014 Terms of Use: http://spiedl.org/terms